Structure-dependent electronic properties of nanocrystalline cerium oxide films

P. Patsalas* and S. Logothetidis
Aristotle University of Thessaloniki, Department of Physics, Solid State Physics Section, GR-54124 Thessaloniki, Greece

L. Sygellou and S. Kennou
Department of Chemical Engineering, University of Patras and FORTH-ICEHT, Rion University Campus, GR-26500 Patras, Greece
(Received 23 December 2002; published 7 July 2003)

We investigate the electronic properties of nanocrystalline cerium oxide (CeO_x) films, grown by various techniques, and we establish universal relations between them and the film structure, composition, and morphology. The nanocrystalline CeO_x films mainly consist of CeO_2 grains, while a considerable concentration of trivalent Ce^{3+} is distributed at the CeO_2 grain boundaries forming amorphous Ce_2O_3. A small portion of Ce^{3+} is also located around O-vacancy sites. The optical properties of the CeO_x films are considered, taking into account the reported band-structure calculations. The fundamental gap E_g of CeO_x is due to the indirect $O2p \rightarrow Ce4f$ electronic transition along the L high-symmetry lines of the Brillouin zone and it is correlated with the $[Ce^{3+}]$ content, explaining the redshift of E_g in nanostructured CeO_x, which is due to the Ce^{3+} at the grain boundaries and not due to the quantum-size effect itself. We also correlate the energy position of the $O2p \rightarrow Ce4f$ electronic transition, which varies up to 160-meV wide, with the lattice constant of the CeO_2 grains. We also show that the higher-order transitions are more sensitive to film composition. The refractive index, far below E_g, is explicitly correlated with the film density, independently of the Ce^{3+}/Ce^{4+} and O concentrations, grain size, and lattice parameter. The density is also found to be the major factor affecting the absolute value of the ε_2 peak, which corresponds to the $O2p \rightarrow Ce4f$ electronic transition.

DOI: 10.1103/PhysRevB.68.035104 PACS number(s): 78.66.Nk, 78.67.Ch, 61.10.Kw, 79.60.Jv

I. INTRODUCTION

Cerium oxides have recently attracted much interest due to their unique properties, which make them suitable for various applications. The valence of Ce is very important for the structure of cerium oxides; tetravalent Ce forms cerium dioxide (CeO_2),[1,2] commonly called ceria, which has a cubic fluorite lattice ($Fm3m$ space group), while trivalent Ce forms the sesquioxide Ce_2O_3, which has a hexagonal lattice ($P\bar{3}m1$ space group).[1,3] Both cerium oxides are refractory compounds, which are optically transparent in the visible spectral region and highly absorbing in the ultraviolet region.[1,4] However, in bulk cerium oxides the existence of trivalent Ce^{3+} has been considered to reduce the band gap.[5]

The most common of cerium oxides is CeO_2, which is stable even in substoichiometric form (CeO_{2-x}, $0 \leqslant x \leqslant 0.4$) (Ref. 6) and thus has been easily produced by several growth techniques. Among them are electron-beam evaporation (EBE),[7–9] pulsed laser deposition,[10–15] metalorganic chemical vapor deposition,[16] ion-beam-assisted deposition (IBAD),[6,17] and reactive magnetron sputtering (RMS).[18–20] Thin films of CeO_2 exhibit unique physical properties, such as a lattice constant ($\alpha = 0.541$ nm) similar to that of Si (making it suitable for epitaxial insulating layers for Si-device technology), a high refractive index, and a high dc dielectric constant. Therefore, CeO_2 films are appropriate for applications in optical,[4,7,21] electro-optical,[8,9] microelectronic,[7,12,16,18,22,23] and optoelectronic[19] devices. Their exceptional optical performance has led to the extensive study of the electronic properties of thin-film and nanostructured CeO_2.[4,10,20,24–28] However, the relative results in the literature are still controversial. For example, nanostructured CeO_2 is reported to exhibit a lower fundamental gap than crystalline CeO_2, although the quantum-size effects are expected to induce a blueshift of the band gap[29,30] due to the more localized bands. In addition, most of the reports correlate the values of optical constants, such as the refractive index (n) (reported to vary between 1.6 and 2.5 at 633 nm), fundamental gap (2.5 to 3.3 eV), and energy position of the $O2p \rightarrow Ce4f$ electronic transition, only with the growth technique and conditions. Therefore, a detailed understanding of the effect of physical properties and microstructure on the optical performance and electronic properties of nanostructured cerium oxides has not yet been established.

In this work we present an effort to investigate the microstructural features, which affect the electronic properties of nanostructured cerium oxide (CeO_x) films. For this purpose a very detailed complementary study of the crystal structure (CeO_x phases and cell sizes), morphology (density, grain size, and defect distribution such as oxygen vacancies, grain boundaries, and voids), and composition (oxygen, trivalent Ce^{3+}, and tetravalent Ce^{4+} contents) has been carried out using well-established characterization techniques such as x-ray diffraction (XRD), x-ray photoelectron spectroscopy (XPS), and x-ray reflectivity (XRR), the latter being a modern technique for the study of thin films in terms of density, surface, and interface roughness.[10,31–33] For our study we have grown CeO_x films using two different growth techniques, EBE and IBAD, and we compare our results with the optical data of epitaxial CeO_2 films produced by RMS and reported by Guo *et al.*[20] and with the reported band-structure calculations for CeO_2 and Ce_2O_3,[1] in order to establish universal relations between the optical properties and the microstructure of the CeO_x films, which are general and valid for any growth process.

The electronic properties of the various CeO_x films are studied by spectroscopic ellipsometry (SE) data analysis. Three methods of analysis are used. The first is the use of the three-phase model (air/film/substrate) (Ref. 34 and 35) in combination with the Tauc-Lorentz model[36] in order to describe and quantify the contributions of the major $O2p \rightarrow Ce4f$ and $O2p \rightarrow Ce5d$ electronic transitions of CeO_2 and the $Ce4f^0 \rightarrow Ce4f^1$ transition of Ce_2O_3 (Ref. 5) and to determine the values of refractive index n of CeO_x for energies below the fundamental gap E_g.[10] The second method is based on Bruggeman's effective medium theory,[34,37] which is used to investigate the effect of the film's density and voids content to n (for $E<E_g$) and to the absolute values of the dielectric function's peak, which corresponds to the $O2p \rightarrow Ce4f$ electronic transition. The third method of analysis of the optical data is through the formulation developed by Tauc, Grigrovici, and Vancu[38] for the description of the dielectric function at energies close to the band gap, using the so-called Tauc plots, in order to determine accurately the fundamental gap of various CeO_x films. Additional ultraviolet photoelectron spectroscopy (UPS) experiments were carried out to study the density of states (DOS) of the valence band of representative CeO_x films.

We found that the nanostructured CeO_x films mainly consist of CeO_2 grains, while a considerable concentration of trivalent Ce^{3+} has been also observed. The trivalent Ce^{3+} is distributed at the CeO_2 grain boundaries forming amorphous Ce_2O_3. A small portion ($<5\%$) of Ce^{3+} is also located around O-vacancy sites. We explicitly correlate the CeO_2 (and Ce_2O_3) content with the value of the fundamental gap E_g of CeO_x. Since cerium oxides exhibit both a direct and an indirect gap, we identify as E_g the indirect gap of the $O2p \rightarrow Ce4f$ transition, which is located $\sim$0.5-eV below the direct gap. The correlation of E_g with the film composition explains the redshift of E_g in nanostructured CeO_x,[4] which is due to the Ce^{3+} at the grain boundaries and not to the grain-size (quantum-size) effect itself. We also correlate the energy position of the $O2p \rightarrow Ce4f$ interband transition, which varies up to 160-meV wide, with the lattice constant of the CeO_2 grains. Finally, the refractive index, far below E_g, is explicitly correlated with the film density according to classical dispersion theory,[39] independently of the Ce^{3+}/Ce^{4+} and O concentrations, grain size, and lattice parameter, revealing that density is the key factor affecting n. In addition, we show that density is also the major factor affecting the absolute value of the ε_2 peak, which corresponds to the $O2p \rightarrow Ce4f$ electronic transition of CeO_2.

II. EXPERIMENT

Three sets of CeO_x films were grown on c-Si(001) substrates in an ultrahigh vacuum (UHV) chamber (base pressure $<1\times10^{-9}$ Torr). The first set consisted of CeO_x samples, 110–170-nm thick, grown by electron-beam evaporation at different substrate temperatures T_s (RT–950 °C). A double electromagnet assembly was used for the surface scan of CeO_2 chunks by a 40–50-mA/7-kV electron beam. The vapor pressure of CeO_2 under these conditions was $1-3\times10^{-5}$ Torr and was monitored and controlled by a quadrapole mass spectrometer. The second set of samples was grown by EBE with similar growth conditions as the samples of the first set, but with higher thickness ($\sim$0.5 μm), in order to better study their bulk properties and compare them directly with the IBAD-produced samples. The third set consisted of CeO_x films, about 0.5-μm thick, grown by IBAD at RT. IBAD growth was realized by evaporation of CeO_2, using a 150–200-mA/7-kV electron beam (providing a vapor pressure of $1-4\times10^{-4}$ Torr), and subsequent bombardment with a focused Ar^+-ion beam generated at a Kauffman broad-beam ion source. The varying parameter at this set of experiments was the Ar^+-ion energy, which was either 0.75 or 1.25 keV. The evaporation rate and the Ar^+ flow rate were varying in order to retain a relative flux of ions arriving (ion/neutral ratio) at $\Phi_{Ar^+}/\Phi_{CeO_x} \cong 0.5$.

The optical properties of the deposited films were measured *ex situ* at RT using a JOBIN-YVON phase-modulated spectroscopic ellipsometer, in the energy range 1.5–5.5 eV with a step of 10 meV at a 70° angle of incidence. UPS experiments were carried out in a UHV chamber equipped with a hemispherical electron energy analyzer (SPECS LH-10) and a discharge lamp (He II radiation with photon energy 20.66 eV). The spectrometer was calibrated using the Fermi edge position of a sputter-cleaned Au foil, which was defined as zero binding energy of the spectra.

XRR/XRD experiments were conducted in a Siemens D-5000 diffractometer equipped with a Goebel mirror,[40] which transforms the divergent x-ray beam parallel to 200-μm width. The XRD scans were performed in Bragg-Brentano geometry between 5° and 60°. The source was a conventional Cu K_α 2.2-kW x-ray tube. The generator current and voltage were 40 mA and 40 kV, respectively, the step was 0.02°, and the scan speed was 0.1°/ min. By taking rocking curves of the reflected x-ray beam from the specimen (at angles lower than the critical angle for total external reflection) we calibrated the goniometer with an accuracy of 0.001°. The XRR measurements were performed in the form of θ-2θ locked couple scans between 0 and 3° using the same x-ray apparatus and a special reflectivity sample stage. XRR scans with a 0.1° offset of the detector were conducted to subtract the contribution of the diffuse scattering from the specular XRR scan.

The XPS experiments were performed in a stainless-steel turbopumped UHV chamber (base pressure $\sim5\times10^{-10}$ Torr). The chamber was equipped with a Leybold LHS-12 hemispherical electron energy analyzer and a nonmonochromatized dual anode x-ray source for XPS. The data were obtained by using the Al K_α radiation at 1486.6 eV and detection normal to the surface with a constant analyzer pass energy of 100 eV, which resulted in an analyzed area of 2×3 mm^2. The binding-energy scale of the spectrometer was referenced to the $Au4f_{7/2}$ value at 84.05 ± 0.05 eV. In all speciments the wide scan spectrum shows that the main peaks are O, Ce, and carbon contamination due to air exposure before introduction to the UHV chamber.

III. RESULTS AND DISCUSSION

A. Film microstructure

XRD and transmission-electron microscopy (TEM) (TEM results are not shown here) were used to study the micro-

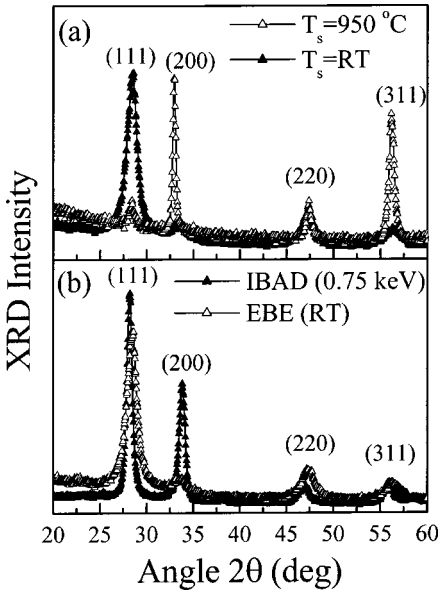

FIG. 1. Representative XRD patterns from representative CeO_x films (EBE and IBAD produced), showing the nanocrystalline character of the films and the cubic fluorite structure of CeO_2. The Miller indices, which correspond to the XRD peaks of CeO_2, are also shown.

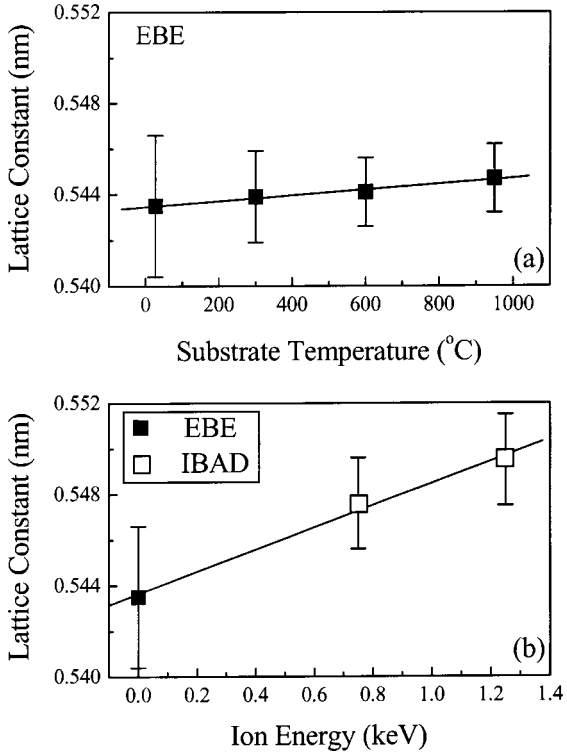

FIG. 2. The lattice constant of the CeO_2 grains, calculated using Eq. (2), vs the major growth conditions of EBE and IBAD (the straight lines are guides to the eye).

structure of the various CeO_x films. Both techniques revealed the polycrystalline character of the CeO_x films, showing broad diffraction peaks (XRD) and diffraction rings (TEM), which are the characteristic patterns of nanocrystalline materials. The films exhibit columnar structure. The columns are polycrystalline and consist of nanoscale grains (9–28 nm). For the quantitative analysis of the film microstructure we used the XRD diffractograms in order to ensure the nondestructive character of the study, because the use of energetic electron beams (such as in TEM) may cause desorption of oxygen from CeO_2 and formation of Ce_2O_3.[2]

The XRD diffractograms revealed the cubic fluorite structure of CeO_2 (Ref. 41) in all films (deposited either by EBE or IBAD). For example, Fig. 1 shows XRD patterns from representative CeO_x films with the assignment of the corresponding Miller indices of the CeO_2 XRD reflections. The XRD peaks have been fitted by pseudo-Voigt curves in order to determine their angular position, broadening, and intensity. The different growth techniques and conditions affect the broadenings and the relative intensities of the various XRD peaks due the variations of grain size and orientation, respectively. No sign of crystalline Ce_2O_3 was detected by XRD. However, XPS had detected a considerable portion of Ce^{3+}, as we show below, suggesting that the Ce_2O_3 phase is amorphous.

The mean grain size G of CeO_2 can be determined from the broadening full width at half maximum$_{hkl}$ (FWHM)$_{hkl}$ of the XRD peaks, which correspond to the lattice planes with Miller indices (hkl), through Scherrer's formula:[42]

$$G = \frac{0.9 \cdot \lambda}{\mathrm{FWHM}_{hkl} \cdot \cos\theta_{hkl}}, \tag{1}$$

where θ_{hkl} is the Bragg angle that corresponds to the (hkl) lattice planes and λ is the x-ray wavelength. For the determination of G we used the broadening of the (111) XRD reflection, which is manifested at lower angular values and thus is less affected by the $k_{\alpha 1}$ and $k_{\alpha 2}$ splitting of the incident beam [except for the film deposited by EBE at 950 °C where we used the (002) reflection because this film was grown along this direction and exhibited a weak (111) peak]. However, we note here that Scherrer's formula is valid for unstrained grains because the strain effects may broaden the XRD peaks, as well. Therefore, before applying Eq. (1) to determine the mean grain size of the CeO_2 nanostructures, we should calculate the lattice constant α.

The lattice constant α of the cubic fluorite-type CeO_2 grains can be determined through the spacing of the (hkl) lattice planes (d_{hkl}), and taking into account Bragg's law:

$$d_{hkl} = \frac{\alpha}{\sqrt{h^2+k^2+l^2}} \Rightarrow \alpha = \frac{\lambda \cdot \sqrt{h^2+k^2+l^2}}{2 \cdot \sin\theta_{hkl}}. \tag{2}$$

Figure 2 shows the calculated lattice constant values vs T_s and ion energy for the EBE and IBAD films, respectively. In Fig. 2(b) the point at $E=0$ keV corresponds to a ~500-nm-thick film produced by EBE at RT (i.e., with conditions and thicknesses similar to IBAD for $E=0$ keV). The lattice constant of all the films has been found to be slightly larger than the corresponding value of bulk ceria,[41] showing that all the films are in-plane compressed. The relative strain s values can be estimated from the calculated lattice constants: s

$=(\alpha-\alpha_{\text{bulk}})/\alpha_{\text{bulk}}$, where α_{bulk} is the lattice constant of the bulk, unstrained ceria.[41] The relative strain for all EBE and IBAD films has been determined to be lower than 0.7% and 1.6%, respectively. The observed strain in CeO_2 grains is due to growth-related processes such as the development of thermal stresses (for films grown by EBE at $T_s > \text{RT}$) and the compressive stresses developed by the intense ion bombardment during ion-assisted growth of refractory compounds (for IBAD).[43] Nevertheless, the s values are very low and thus their effect on FWHM_{hkl} is minor and Scherrer's formula can be used to estimate the grain size of CeO_2.

The grain size of EBE-grown films increases with T_s (from 9 to 24 nm) due to the higher mobility of the adatoms during growth.[43] The IBAD-grown films exhibit relatively bigger grains (23–28 nm) either due to their thickness (~500 nm, instead of the 110–170-nm thickness of the EBE-grown films) or the energy transport from the inert gas ions to the Ce and O adatoms at the film surface during growth, which results in similar effects as those of increased T_s.[43] Nevertheless, the origin of the grain-size values does not affect the following study, because we correlate directly the electronic properties with the structural features (composition, grain size itself, etc.) of CeO_x films, independently of the growth technique and film thickness.

Another microstructural feature, which considerably affects the optical properties of CeO_x, is the film density.[10] The film density can be determined by XRR through the critical angle θ_c for total external reflection of x rays, which can be expressed in terms of the mass density ρ:[31]

$$\theta_c^2 = \left(\frac{e^2\lambda^2}{\pi m c^2}\right)\cdot\left(N_o\frac{Z_t}{A_t}\right)\cdot\rho, \tag{3}$$

where m, e are the electron mass and charge, respectively, N_o is Avogadro's number, A_t is the mean atomic mass, λ the x-ray wavelength, and Z_t the mean number of electrons (sum of core, valence, and conduction electrons) per atom.

The XRR measurements were analyzed using Siemens REFSIM software and a Monte Carlo (MC) algorithm.[31] Figure 3(a) shows the XRR curve and the results of the MC fitting for a CeO_2 film, 112-nm thick, deposited at 950 °C. The calculated density (6.7 g/cm^3) is smaller than the density of the bulk CeO_2 (7.21 g/cm^3),[44] due to the polycrystalline character of the films and the existence of voids. The voids content in the film may be estimated from the density, taking into account, its value for bulk CeO_2.[41,43] The XRR curves of two CeO_x films deposited by EBE at RT and 950 °C are compared in Fig. 3(b). The film deposited at RT is much less dense (4.5 g/cm^3). Figure 4 illustrates the densification and elimination of voids with T_s, due to the higher mobility of the adatoms during growth, which results in more compact stacking and close-packed structures.[31,43] The films grown by IBAD are much denser (ρ up to 6.1 g/cm^3) than the films grown by EBE at RT. This densification is a typical effect of ion bombardment during growth of refractory compounds.[31,43] XRR has also determined the surface roughness of the films, which varies in the range 3–4 nm. These values are much lower than those reported in the literature.[20] The surface-roughness values of our films are not correlated with any other film characteristic (thickness, density, grain size), and they may possibly be attributed to a top nucleation layer as has been observed in Si growth.[44]

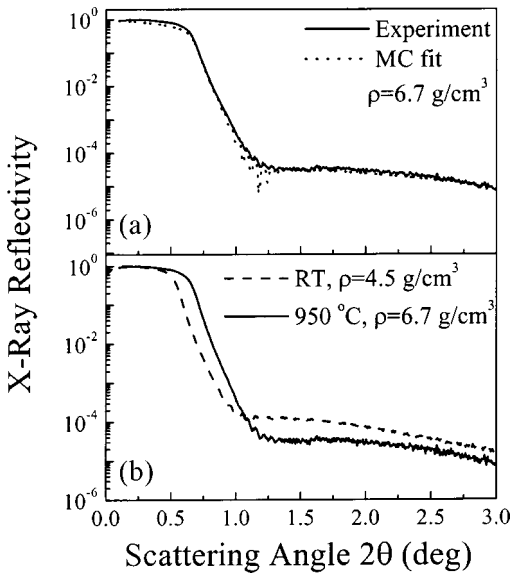

FIG. 3. (a) XRR data from a CeO_x film grown by EBE at 950 °C and the results of the MC fitting and (b) comparison of XRR data of two CeO_x films deposited by EBE at RT and 950 °C.

The film composition has been studied by XPS. XPS observed the characteristic O1s and Ce3d peaks, from which the film stoichiometry and bonding type can be determined. Figure 5 displays the core levels of Ce3d of two representative films grown by EBE and IBAD; the characteristic peaks in which the Ce3d states are analyzed are indicated by the vertical dotted lines. The Ce3d spectrum of CeO_x can be fully described by six peaks of three spin-orbit doublets.[45–48] The assignments of these peaks and the reference values for their binding energies have been a subject of intense research and much data are available in the literature.[45–49]

Figure 5 also shows the fitted deconvolution of the Ce3d levels to the various states, in addition to the experimental XPS data. The observed XPS peaks are attributed to trivalent Ce^{3+} and tetravalent Ce^{4+}. The peaks, which correspond to

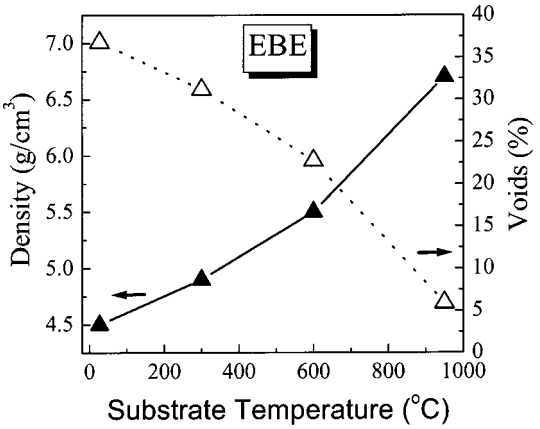

FIG. 4. The variation of density and voids content with T_s for the EBE-grown films.

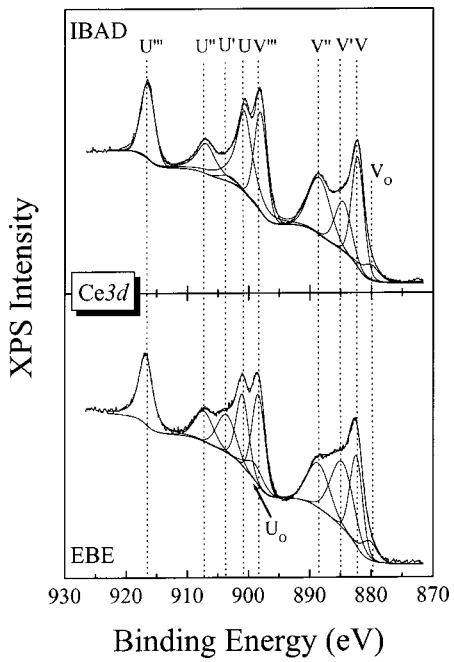

FIG. 5. The Ce3d core levels for representative CeO_x films grown by IBAD and EBE. The fractions of Ce^{3+} and Ce^{4+} can be determined from the Ce3d XPS peaks, showing that the IBAD-produced films exhibit a higher Ce^{4+} content.

Ce^{4+} are the U''' (916.7 eV) and V''' (898.4 eV), which result from the Ce3d^9 O2p^6 Ce4f^0 final states. The additional states of Ce^{4+} [U (901.0 eV), V (882.5 eV), U'' (907.3 eV), V'' (888.8 eV)] result from a mixture of Ce3d^9 O2p^5 Ce4f^1 and Ce3d^9 O2p^4 Ce4f^2 final states. The transfer of electrons from the O2p to the Ce4f orbital and the decrease in the Ce3d binding energy are due to the interaction of the Ce4f level with the Ce3d core hole, which pulls the Ce4f level to lower energy. Finally, the contribution of Ce^{3+} to the Ce3d spectrum consists of two doublet pairs: (i) U' (903.5 eV)/V' (884.9 eV) and (ii) U_o (898.8 eV)/V_o (880.3 eV). These doublets correspond to a mixture of the Ce3d^9 O2p^5 Ce4f^2 and Ce3d^9 O2p^6 Ce4f^1 final states.

For the quantitative determinations of the $[Ce^{3+}]/[Ce^{4+}]$ ratio we used two methods: (i) the method that proposed by Shyu *et al.*,[50] in which the area of the whole Ce3d multiplet is linearly correlated with the ratio $Ce^{3+}/(Ce^{3+}+Ce^{4+})$; in this case the decrease of U''' indicates the increase in Ce^{3+} species due to the Ce^{+4} reduction. (ii) The second method uses directly the ratio of the intensities of Ce^{4+} and Ce^{3+} peaks. The results of the two methods are in very good agreement and reveal the existence of a considerable concentration of Ce^{3+}, although XRD identified only the tetravalent CeO_2. The results of the XPS analysis are summarized in Table I. The trivalent Ce^{3+} can be distributed either in regions of sesquioxide Ce_2O_3 (Ref. 1) or around O vacancies in CeO_2.[5]

In order to investigate if the trivalent Ce^{3+} has the form of Ce_2O_3 or is due to O vacancies, we calculated the O content in the film assuming that the total O content is the sum of the required O to fully oxidize Ce^{4+} and Ce^{3+} and to form CeO_2 and Ce_2O_3, respectively. Then, taking into account that the stoichiometry $x=[O]/[Ce]$ is equal to 2 for CeO_2 and 1.5 for Ce_2O_3, the ratio of the required oxygen to fully oxidize Ce^{4+} and Ce^{3+} to the sum $[Ce^{4+}]+[Ce^{3+}]$ is determined from the concentrations $[Ce^{4+}]$ and $[Ce^{3+}]$ according to the following equation:

$$x=\frac{[O]}{[Ce]}=\frac{3}{2}\times[Ce^{3+}]+2\times[Ce^{4+}]. \quad (4)$$

The calculated stoichiometry from Eq. (4) has been compared with the stoichiometry determined directly from the intensities of the O1s (with binding energy 529.5 eV) and Ce3d XPS peaks. Figure 6 shows the stoichiometry variations with the concentration of $[Ce^{3+}]$ determined by both methods (requiring O to fully oxidize Ce^{3+} and Ce^{4+} and direct comparison of the O1s and Ce3d XPS peak intensities). The two methods are in excellent agreement for films exhibiting low $[Ce^{3+}]$ content, meaning that in these films the entire $[Ce^{3+}]$ content is consumed in forming Ce_2O_3. On the other hand, we observe a slight O deficiency (with respect to the required O needed to fully oxidize Ce) in the films with high $[Ce^{3+}]$ content, suggesting that Ce_2O_3 and O vacancies coexist in these films. However, the maximum O deficiency is less than 5% and thus the majority (>95%) of $[Ce^{3+}]$ is consumed in Ce_2O_3 in any case.

XPS provided evidence that Ce_2O_3 exists in the nanostructured CeO_x films, while XRD identified only CeO_2.

TABLE I. The composition, density, and energy positions of E_g and the O2$p\rightarrow$Ce4f electronic transition (E_{01}) for the various CeO_x films with respect to the growth technique and conditions.

	T_d (°C)	E_i (keV)	$[Ce^{4+}]/[Ce^{3+}]$	$[O]_{O1s}/[Ce]_{Ce3d}$[a]	$[O]/[Ce]_{Ce3d}$[b]	E_g (eV)[c]	E_{01} (eV)	ρ (g cm^{-3})
EBE	950		4.9	1.91	1.92	3.05±0.18	3.91±0.04	6.7
	600					2.99±0.18	3.97±0.04	5.5
	300		3.8	1.85	1.90	2.94±0.15	3.94±0.05	4.9
	RT		3.0	1.80	1.88	2.92±0.04	4.02±0.04	4.5
IBAD	RT	1.25	4.3	1.89	1.91	2.97±0.06	3.85±0.02	5.9
	RT	0.75	6.4	1.96	1.94	3.12±0.06	3.94±0.02	6.1

[a]Using directly the intensities of the O1s and Ce3d XPS peaks.
[b]From Eq. (4), using the deconvolution of the Ce3d XPS peak.
[c]Using Eq. (10).

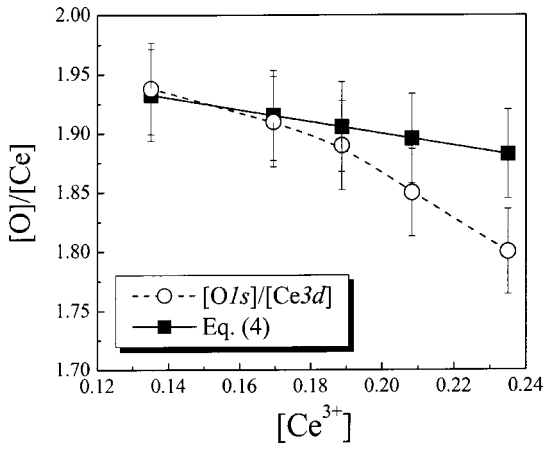

FIG. 6. The CeO_x stoichiometry (for both EBE- and IBAD-grown films) calculated (a) directly from the intensities of the O1*s* and Ce3*d* XPS peaks (open circles) and (b) from the concentrations of Ce^{3+} and Ce^{4+} (solid squares), assuming that Ce^{3+} and Ce^{4+} exclusively form Ce_2O_3 and CeO_2, respectively.

Therefore, the Ce_2O_3 phase is amorphous. The amorphous character of Ce_2O_3 is an indication that this phase is located at the grain surface and at the grain boundaries. Following simple dimensional analysis we determine that if Ce_2O_3 and CeO_2 are located at the grain surface and volume, respectively, then the square of $[Ce^{3+}]$ (surface distribution) will be linearly correlated with the third power of $[Ce^{4+}]$ (grain volume distribution). Indeed, Fig. 7 shows the correlation of the square of $[Ce^{3+}]$ ($\cong[Ce_2O_3]$) with the third power of $[Ce^{4+}]$ ($=[CeO_2]$) and the third power of G (which is proportional to grain volume V_g). The observed linear relation

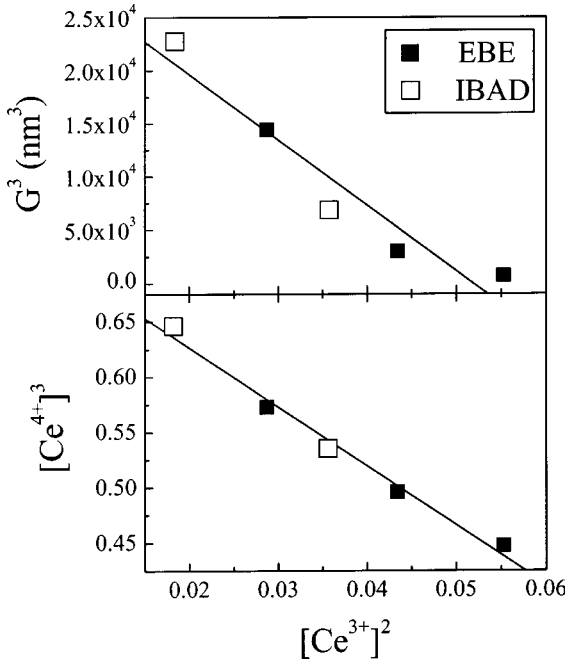

FIG. 7. The correlation of the square of the Ce^{3+} concentration with the third power of the Ce^{4+} concentration and the grain volume ($V_g \propto G^3$), showing that Ce^{3+} and Ce^{4+} are located at the grains' surface and volume, respectively.

between $[Ce^{3+}]^2$ and $[Ce^{4+}]^3$ confirms the dimensional analysis and the distribution of CeO_2 and Ce_2O_3 at the grain volume and surface, respectively. The experimental points of G^3 vs $[Ce^{3+}]^2$ are more scattered around the straight line of the dimensional analysis. This is attributed to the strain of the grains that affects the broadening of the XRD peaks and the determined grain-size values.

B. Electronic properties

After studying in detail the microstructure and morphology of CeO_x films, we proceed to the study of their optical properties. The optical properties of the CeO_x films have been investigated by SE in the visible UV spectral region (1.5–5.5 eV). The main benefit of the ellipsometric measurements (compared to other optical measurements) is the direct evaluation of both the real and imaginary parts of the complex dielectric function $\varepsilon(\omega)=[\varepsilon_1(\omega)+i\varepsilon_2(\omega)]$, through the ellipsometric angles Ψ and Δ, with no need for Kramers-Kronig integration.[35] The determination of the complex dielectric function enables the investigation of the material's electronic structure [$\varepsilon_2(\omega)$ is directly related to the joined density of states (JDOS) for interband absorption]. The material's electronic structure [and consequently the determined $\varepsilon(\omega)$] is very sensitive to the materials' microstructure, since small grains may induce quantum-size effects,[29,30] the point defects may create localized states within the band gap,[5] and in mixed materials (such as CeO_2/Ce_2O_3) the various phases may have different electronic structures band gaps,[1] etc.

In the case of transparent films the measured quantity is the pseudodielectric function $\langle\varepsilon(\omega)\rangle$, which takes into account contributions from the substrate and the film's thickness due to the multiple reflections originating from the film-substrate interface.[35] Such intense multiple reflections are manifested in the $\langle\varepsilon(\omega)\rangle$ spectra (Fig. 8) of CeO_x films for photon energy $E=\hbar\omega<E_g$, meaning that all the CeO_x films are highly transparent for $E<3$ eV, regardless of their thickness values (in Fig. 8, the dashed and dotted lines correspond to EBE-grown thin films of the first set, while the solid line corresponds to a thick ~500 nm IBAD-grown film). For photon energy $E>E_g$ ($\cong$3 eV) optical absorption begins and the Si substrate contribution to $\langle\varepsilon(\omega)\rangle$ is reduced, even for the thinner film (EBE grown, 950 °C, dotted line).

The second part ($E>3$ eV) of the SE spectra is dominated by an absorption peak at ~4 eV, which corresponds to the $O2p\rightarrow Ce4f$ transition[1,5,10,20,51] of CeO_2, according to the calculated band structure and DOS (Ref. 1) shown in Fig. 9. In particular, the fundamental gap of the CeO_x films is due to indirect $O2p\rightarrow Ce4f$ transitions of CeO_2 along the L high-symmetry lines of the Brillouin zone denoted by arrows in Fig. 9. This point is discussed in more detail in the following paragraphs. The $O2p\rightarrow Ce4f$ transition is very sharp due to the low energy broadening of the $Ce4f$ band.[1,5] Many authors refer to the $Ce4f$ state as an atomiclike localized band into the band gap between the $O2p$ valence band and the extended $Ce5d$ conduction band,[1,2,19,49] defining as the CeO_2 band gap the energy separation between the $O2p$ and $Ce5d$ states, which is about 6 eV.[2,5,19,49] Nevertheless, the $O2p\rightarrow Ce4f$ transition is attributed exclusively to CeO_2, because

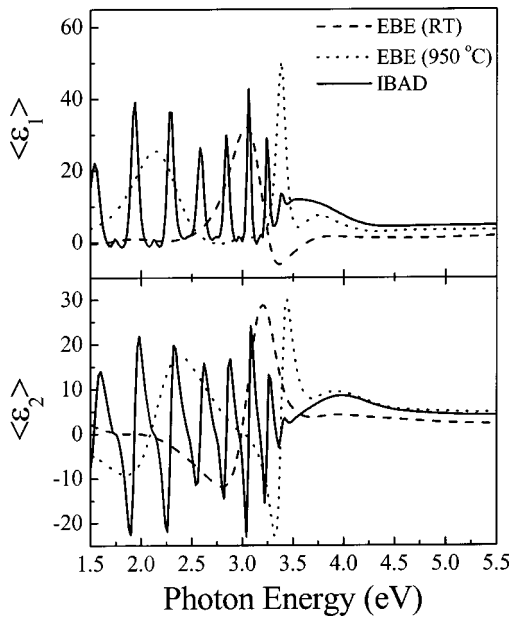

FIG. 8. SE measurements of $\langle\varepsilon(\omega)\rangle$ from representative CeO_x films grown by IBAD and EBE (to different thicknesses). All films are highly transparent below 3 eV, where intense multiple reflections are manifested. An absorption peak appears at ~4 eV, which is due to a $O2p \rightarrow Ce4f$ electronic transition of CeO_2.

in Ce_2O_3 the $Ce4f^0$ band is partially filled with valence electrons[1] and thus only higher-order transitions occur in Ce_2O_3. The maximum value of the ε_2, which corresponds to the $O2p \rightarrow Ce4f$ interband transition, has been a subject of intense debate[1,5,20,51] and varies considerably in our films (see Fig. 8). This point is also discussed thoroughly in the following text. Finally, for $E > 4$ eV the dielectric function is also affected by the contribution of the low-energy tails of the $O2p \rightarrow Ce5d$ interband transition of CeO_2 and the $Ce4f^0 \rightarrow Ce4f^1$ transition of Ce_2O_3.[2,49]

In order to evaluate the spectral dependence of the dielectric function of CeO_x films, we fitted the experimental $\langle\varepsilon(\omega)\rangle$ using the modified Tauc-Lorentz (TL) model,[36] in combination with the three-phase model (air/CeO_x film/c-Si substrate). In the TL model the imaginary part $[\varepsilon_2(\omega)]$ of the dielectric function is determined by multiplying the Tauc JDOS (Ref. 38) by the ε_2 obtained from the Lorentz oscillator model.[39] Thus, the TL model provides the ability to determine the fundamental optical gap E_g of the electronic transitions, in addition to the energy E_0, broadening C, and strength A of each Lorentz oscillator.[39] The energy E_0 of this model corresponds to the Penn gap, where the strong absorption of the material takes place. The imaginary part ε_2 of a TL oscillator is described by the following expressions:[36]

$$\varepsilon_2(E) = \frac{AE_0C(E-E_g)^2}{(E^2-E_0^2)^2+C^2E^2}\cdot\frac{1}{E}, \quad E > E_g. \tag{5a}$$

$$\varepsilon_2(E) = 0, \quad E \leqslant E_g, \tag{5b}$$

and the real part ε_1 is obtained by Kramers-Kronig integration.[36,39]

$$\varepsilon_1(E) = \varepsilon_\infty + \frac{2\hbar^2}{\pi} P \int_{\omega_g}^{\infty} \frac{x\varepsilon_2(x)}{x^2-E^2}\,dx. \tag{6}$$

The parameter ε_∞ is larger than unity and accounts for the contributions from electronic transitions occurring at energies higher than 8 eV (i.e., $Ce5p \rightarrow Ce5d$ and $Ce5p \rightarrow Ce6s$ transitions[1]) and they have not been taken into account in our analysis with two TL oscillators. The quality of the relative model fit can be judged by the comparison of the experimental and calculated Ψ and Δ and it is based on the minimization of the mean square error χ^2:

$$\chi^2 = \frac{1}{(2N-P-1)}\sum_{i=1}^{N}\{[\Psi_{\text{calc}}(E_i)-\Psi_{\text{exper}}(E_i)]^2 + [\Delta_{\text{calc}}(E_i)-\Delta_{\text{exper}}(E_i)]^2\}, \tag{7}$$

where $2N$ is the number of independent measurements (Ψ and Δ are at N energy positions E_i), P is the number of the free, independent TL-model parameters, and Δ_{calc} (Ψ_{calc}) and Δ_{exper} (Ψ_{exper}) are the calculated and experimental Δ (Ψ) angles at each energy E_i. For the TL fit a Lavender-Marquant minimization algorithm was used to minimize χ^2 with confidence limits 95%. The typical values of χ^2 for the TL fit on the studied CeO_x vary, $0.1 < \chi^2 < 0.4$.

For the TL fits we used two TL oscillators. The first one describes the $O2p \rightarrow Ce4f$ transition (at ~4 eV), which is characteristic of CeO_2 (see Fig. 9). We note here that the so-called $O2p \rightarrow Ce4f$ transition should be forbidden because it violates the angular momentum selection rule ($\Delta l = 0, \pm 1$, where l is the angular momentum quantum number). However, this transition is manifested in all $\varepsilon(\omega)$ spectra of CeO_2 in the literature,[5,10,20,24] because the highest occupied valence band (denoted as the $O2p$ band in Fig. 9) is not exclusively due to $O2p$ electrons because it also contains a contribution from $Ce4d$ electrons, which provide partial d character.[1,5] Therefore, the electronic transition at ~4 eV is a nominal $O2p \rightarrow Ce4f$ transition (and we follow this terminology to be consistent with previous literature) whereas it has actually strong $d \rightarrow f$ ($Ce4d \rightarrow Ce4f$) character, which fulfills the selection rules. We also used a second TL oscillator (at 6.5–8 eV) to describe the low-energy tales of higher-order transitions such as the $O2p \rightarrow Ce5d$ interband transition of CeO_2 and the $Ce4f^0 \rightarrow Ce4f^1$ transition of Ce_2O_3.[2,49] The second TL oscillator averages the contribu-

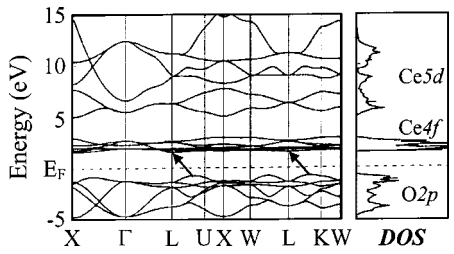

FIG. 9. The band structure and the DOS for pure CeO_2 (after Ref. 1). The arrows indicate the indirect transitions, which correspond to the fundamental gap of CeO_2 and the nanostructured CeO_x films.

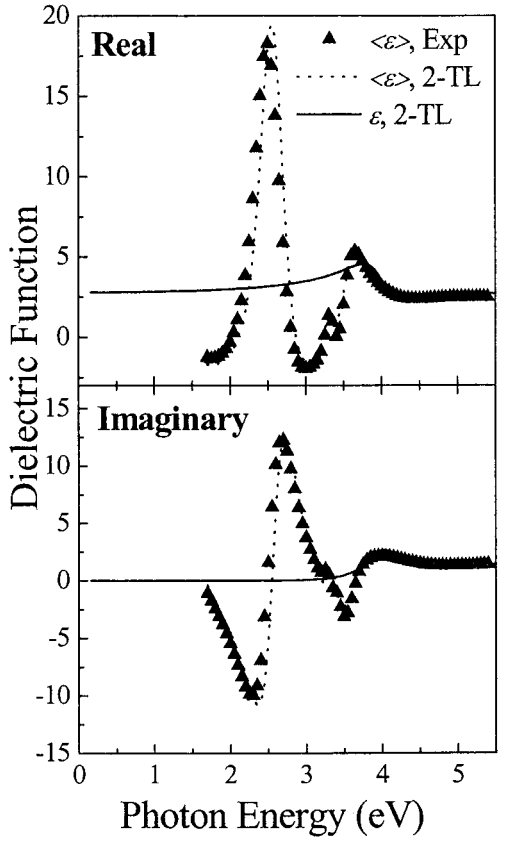

FIG. 10. The experimental ($\langle\varepsilon\rangle$ exper, solid triangles) and fitted curves ($\langle\varepsilon\rangle$ two TL, dotted lines), within the three-phase model, for a representative CeO_x film (EBE at RT), as well as the corresponding ε_1, ε_2 (ε, two TL, solid lines) curves for the bulk material, which were calculated using the best-TL-fit parameters.

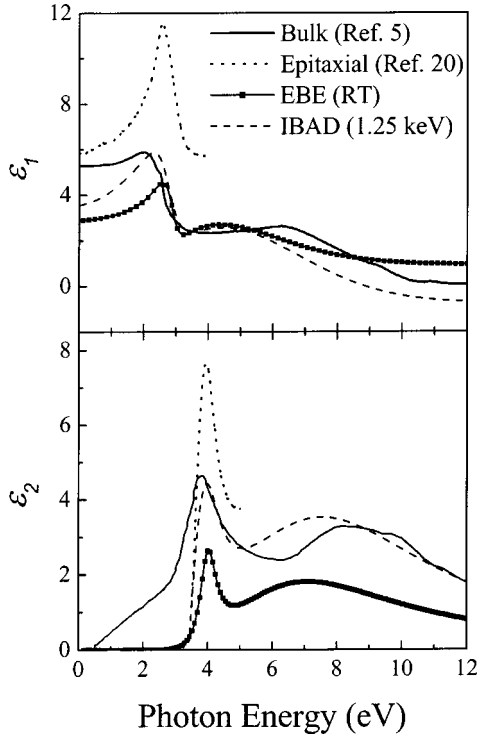

FIG. 11. The calculated $\varepsilon(\omega)$ spectra, based on the two-TL best-fit parameters, for representative CeO_x films. The optical data reported by Marabelli and Wachter for bulk CeO_2 (Ref. 5) and by Guo *et al.* for epitaxial CeO_2 (Ref. 20) are also shown for comparison.

tions of the above-mentioned transitions and their fine structure (which was observed for the $O2p \rightarrow Ce5d$ transition of CeO_2, due to the crystal-field splitting of the $Ce5d$ conduction band to the $Ce5de_g$ and $Ce5dt_{2g}$ subbands[1,5,49,52]). Figure 10 shows representative experimental (exp) and fitted (2 TL), within the three-phase model, $\langle\varepsilon(\omega)\rangle$ curves for a representative EBE-grown CeO_x film, as well as the ε_1, ε_2 curves for the corresponding bulk material, which were calculated based on the best-TL-fit parameters.

The results of the two-TL fits were used to predict and extend the $\varepsilon(\omega)$ curves to lower (0.16 eV) and higher (up to 12 eV) energies than those within the experimental spectral region. The low limit of $E=0.16$ eV is much lower than E_g but higher than the optical absorption at 275 cm^{-1}, which is due to the triply degenerate polar lattice vibrations.[5] Thus, in this analysis we account exclusively for the effect of the electronic transitions and we can evaluate some properties such as the value of the refractive index, ε_1 for $E \ll E_g$ (e.g., the solid line in Fig. 9), and the energy position of the higher-order transitions. However, the predicted $\varepsilon(\omega)$ curves, outside the experimental spectral region, should be considered with particular care, especially in the case of the higher-order transitions, since only the low-energy tails of these transitions contribute to the experimental spectra. Table I summarizes the main results of the two-TL fit analysis, namely, the fundamental gap E_g and the energy position E_{01} of the $O2p \rightarrow Ce4f$ transition, which are included in the experimental spectral region.

Figure 11 shows the calculated $\varepsilon(\omega)$ spectra based on the two-TL best-fit parameters of representative EBE- and IBAD-grown CeO_x films, in comparison with the optical data reported previously for the bulk CeO_2 (Ref. 5) and for epitaxial CeO_2 films.[20] In all $\varepsilon(\omega)$ spectra a strong absorption peak with maximum at $E_{01} \sim 4$ eV, due to an electronic transition, is prominent. According to TL calculations, this transition has been located up to 160 meV (from 3.85 to 4.01 eV). In addition, we did not observe any correlation between the energy positions of this transition with the film composition (CeO_2 and Ce_2O_3 content), proving that this transition originates exclusively from CeO_2, and thus, the Ce_2O_3 regions do not contribute at all, in agreement with the band-structure calculations (Ref. 1 and Fig. 9). On the other hand, we observed a correlation between the energy position E_{01} of the maximum optical absorption of the first TL oscillator with the lattice constant of the CeO_2 grains, which is shown in Fig. 12. This correlation is well understood, since the Brillouin zone (and consequently the energy positions of electronic transitions) reflects the symmetry of the crystal cell, which is its reciprocal. The scattering of the experimental points is due to the very small variations of E_{01} and α as well as to other factors that may affect the energy positions of the interband transitions, such as film thickness, surface roughness, and CeO_2 grain size.

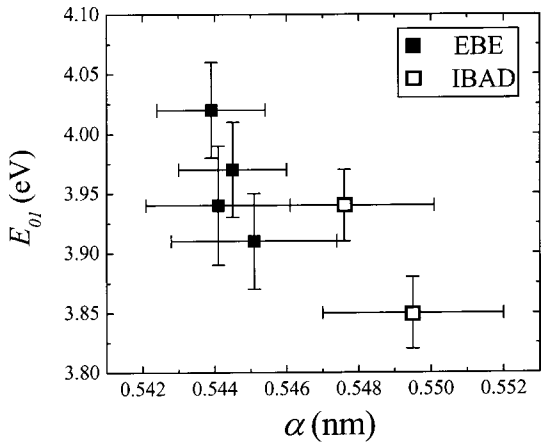

FIG. 12. The energy position of the $O2p \rightarrow Ce4f$ electronic transition of CeO_2 vs the lattice constant of the CeO_2 grains.

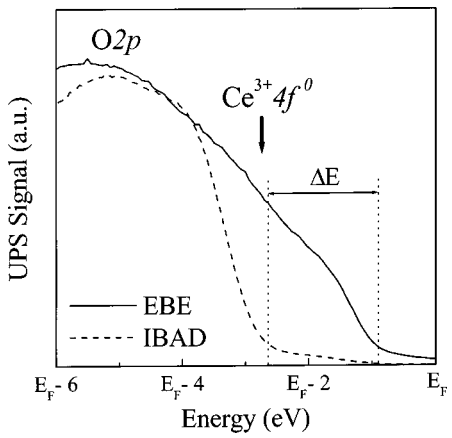

FIG. 13. Valence-band spectra of representative CeO_x films grown by EBE (solid line, $[Ce^{3+}] \cong 0.23$) and IBAD (dashed line, $[Ce^{3+}] \cong 0.13$). The characteristic $O2p$ band is manifested in both spectra and a shoulder attributed to $Ce^{3+}4f^0$ states is more pronounced in the spectrum of the EBE-grown film. The upper edge of the valence band is quite affected by the $Ce^{3+}4f^0$ states.

The energy position E_{02} of the second TL oscillator is very sensitive to the film composition and varies within the range 6.5–8 eV. This is clearly illustrated comparing the ε_2 curves of the EBE- and IBAD-produced films in Fig. 11. The second TL oscillator is located at ~6.5 eV in the case of the Ce_2O_3-rich EBE film and at ~8 eV in the case of the more stoichiometric CeO_2 film grown by IBAD. Comparing these results with the energy position of the $O2p \rightarrow Ce5d$ interband transition, which occurs at ~9 eV for the bulk CeO_2 (Fig. 11, solid line, and Ref. 5), we identify a trend of a strong redshift of the second TL oscillator with increasing Ce_2O_3 content. The observed redshift with increasing Ce_2O_3 content can be very well understood, if we take into account that the second TL oscillator averages the contributions of interband transitions of CeO_2 and Ce_2O_3, and it is in very good agreement with the band-structure calculations, which show that Ce_2O_3 exhibits a lower band gap than CeO_2.[1,52] However, we should mention that the variations (6.5–8 eV) of the second TL oscillator with Ce_2O_3 content are comparable with the error of the E_{02} values calculated by the TL fit (~1.5 eV). The error of the E_{02} values is due to the large broadening of this oscillator in addition to the fact that only the low-energy tail of this oscillator contributes to the experimental spectrum. Therefore, the observed trend cannot be considered as clear evidence but only as a serious indication for the redshift of the second oscillator; further experimental work at higher photon energies is required to confirm this observation.

According to previous studies[2,49] the $O2p \rightarrow Ce5d$ interband transition of CeO_2 is expected to exhibit a Penn gap >8 eV, while the corresponding value of the $Ce4f^0 \rightarrow Ce4f^1$ transition of Ce_2O_3 is around 6 eV. Therefore, the observed redshift of the second TL oscillator should be correlated with the occupancy of the $Ce4f$ states, which are characteristic of Ce_2O_3.

In order to investigate the validity of this argument, we carried out UPS measurements to study the valence band of representative CeO_x films. Figure 13 shows UPS measurements illustrating the valence-band spectra of representative CeO_x films grown by EBE (solid line, $[Ce^{3+}] \cong 0.23$) and IBAD (dashed line, $[Ce^{3+}] \cong 0.13$). The characteristic $O2p$ band is manifested in both spectra [this band is reported to be located around 6-eV below the Fermi level (E_F) (Refs. 2 and 49)] and a shoulder attributed to $Ce^{3+}4f^0$ states [located at about 3-eV below E_F (Refs. 2 and 49)] is more pronounced in the spectrum of the EBE-grown film. The upper edge of the valence band is quite affected by the $Ce^{3+}4f^0$ states.

Indeed, the energy separation between the upper edge of the valence band and E_F is about 1 and 2.6 eV for the EBE- and IBAD-grown films, respectively, due to the more pronounced $Ce^{3+}4f^0$ states in the first film. The valence-band spectra are associated with the DOS and the interband transitions, which, determined by SE data analysis, are associated with JDOS; therefore, no quantitative correlation between the UPS and SE results can be established. However, the UPS results support the SE data analysis, considering that the redshift of the second TL oscillator is attributed to the $Ce4f^0 \rightarrow Ce4f^1$ transition of Ce_2O_3 and it is more pronounced when the valence band exhibits more enhanced $Ce^{3+}4f^0$ features.

In addition to the energy positions of the electronic transitions, another issue that has produced major disagreement in the literature is the maximum value of ε_2 that corresponds to the $O2p \rightarrow Ce4f$ transition at ~4 eV.[1,5,20,51] It has been proposed that this value is majorly affected by the broadening of this transition,[1] however, we have previously shown that the absolute value of the extinction coefficient k (and consequently $\varepsilon_2 = 2nk$) at ~4 eV for CeO_x films is considerably affected by the CeO_x film density.[10] Therefore, the voids content (which degrades the film density) may be the major factor that affects the absolute ε_2 value of the $O2p \rightarrow Ce4f$ transition. In order to investigate the role of voids, we used Bruggeman's effective medium theory (BEMT). For the BEMT analysis we assumed that the dielectric function of CeO_x films consist of contributions of the dielectric functions of pure CeO_2 and voids. This assumption is justified in the spectral region 1.5–4.5 eV, where the dominant $O2p$

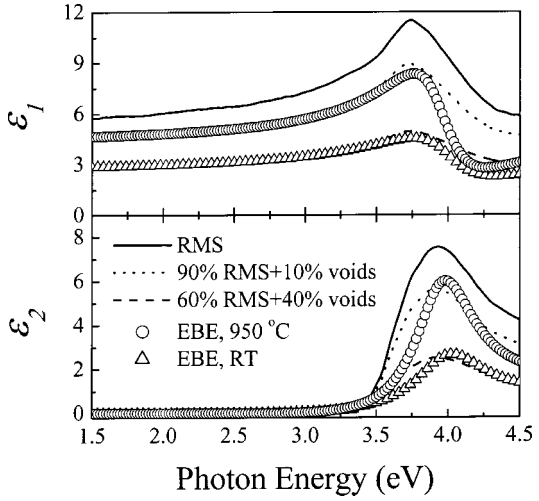

FIG. 14. The optical data reported in Ref. 20 for the epitaxial CeO_2 films grown by RMS (solid line) The results of BEMT simulations for CeO_x films consisted of a material similar to that RMS grown and voids, in comparison with the optical data of the marginal cases of EBE-grown CeO_x (950 °C and RT) determined through the two-TL fittings.

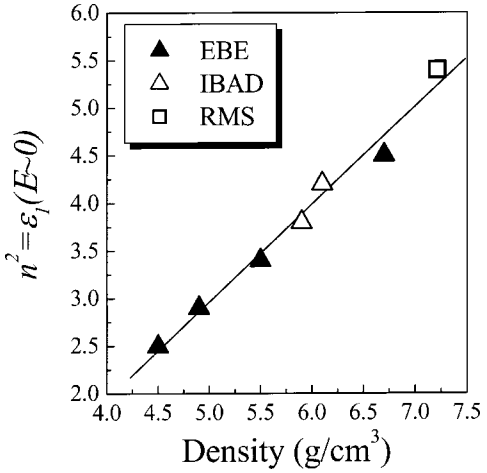

FIG. 15. The square of the refractive index of CeO_x films follows a linear correlation with the film density, which is valid for all CeO_x films grown by EBE, IBAD, and RMS.

$\rightarrow$Ce4f transition comes exclusively from CeO_2 and, thus, the contribution of Ce_2O_3 is minor.

The higher ε_2 values in the litterature have been reported by Guo *et al.*[20] and they correspond to an epitaxial CeO_2 film; they are presented in Fig. 11 in comparison with the ε_2 values of bulk CeO_2 (Ref. 5) and representative EBE- and IBAD-produced CeO_x films of our study. For the BEMT analysis we used their data as the reference dielectric function of pure, single-crystal CeO_2. We determined the dielectric functions of hypothetical CeO_x materials, which consist of single-crystal regions and voids (with various volume fractions of voids), using BEMT. Then, we compared the simulated BEMT results with the dielectric functions of the EBE- and IBAD-grown films, determined through the two-TL fittings. Such dielectric functions simulated by BEMT are presented in Fig. 14 in the spectral region 1.5–4.5 eV. The solid line (refered as RMS) corresponds to the pure RMS-grown CeO_2 of Guo *et al.*,[20] whereas the dotted and dashed lines correspond to hypothetical composite materials (CeO_2+voids) with different voids volume fractions. In addition, we show the optical data of the marginal cases of EBE-grown CeO_x films (950 °C and RT, presented with open triangles and circles exhibiting the highest, 6.7 g/cm^3, and lowest, 4.5 g/cm^3, densities, respectively) determined through the two-TL fittings.

We notice that there is very good agreement between the simulated dielectric functions of the hypothetical composite CeO_x and the dielectric functions of the EBE-grown films for $E<E_g$, suggesting that ε_1 for $E<E_g$ is mainly affected by the film density and less so by other factors such as composition and grain size. The maximum absolute values of the ε_1 and ε_2 for the O2$p\rightarrow$Ce4f transition at $\sim$4 eV, of the two hypothetical, composite CeO_x materials (with 10% and 40% voids volume fractions), are similar to the corresponding values of the two EBE-grown films. The slight differences in the line shapes of the dielectric functions of the hypothetical, composite (CeO_2+voids), and the EBE-grown CeO_x are due to broadening variations, which are attributed to other factors such as film stress.

The voids volume fractions of the two hypothetical composite materials are consistent with the voids calculated by XRR and presented in Fig. 4. The agreement and consistency between BEMT simulations and XRR results suggest that the epitaxial CeO_2 film of Guo *et al.*[20] exhibits density equal to the bulk CeO_2 single crystal.[41] It is very interesting that the values of ε_1 (for $E<E_g$) and the maximum values of ε_1, ε_2 of the various nanocrystalline CeO_x films may be described so well, based exclusively on the dielectric functions of the single-crystal CeO_2. This confirms that the O2$p\rightarrow$Ce4f transition comes exclusively from CeO_2, is not affected by the Ce_2O_3 content in the films at all, and that the voids content (and consequently the film density) is the major factor that determines the maximum value of ε_2 in the O2p $\rightarrow$Ce4f transition.

Based on the previous BEMT analysis we identified a correlation of ε_1 (for $E<E_g$) with the voids volume fraction (equivalent to film density). This is very important for the determination of the refractive index n, which is correlated with ε_1 through the relation $\varepsilon_1=n^2-k^2$. In order to establish an explicit relation between n (for $E<E_g$) and the film density we correlated the n values at 0.16 eV determined by the TL-fit results with the density measured by XRR. The value of n^2 at low energy is equivalent to ε_1, taking into account that $k=0$ for $E<E_g$. The correlation between $\varepsilon_1(E\sim0)=n^2$ and film density ρ is clearly illustrated in Fig. 15. The square of n follows a universal linear relation with ρ for films deposited by EBE, IBAD, and RMS and confirms whether the films are nanocrystalline or single crystal. The RMS point has been determined by fitting the optical data of epitaxial, crystalline CeO_2 reported by Guo *et al.*[20] with the two-TL model, assuming that the density of the single crystal is equal to that of bulk CeO_2 (7.21 g/cm^3), as we have determined using the combined BEMT/XRR analysis.

The linear correlation between n^2 and ρ can be well ex-

plained according to the classical theory of light dispersion.[39] The real part of the dielectric function of a material, which exhibits q electronic transitions, is given by the expression

$$\varepsilon_1(\omega)=1+\frac{4\pi N_e e^2}{m}\sum_{j=1}^{q}\frac{f_j\cdot(\omega_j^2-\omega^2)}{(\omega_j^2-\omega^2)^2+\gamma_j^2\omega^2}, \qquad (8)$$

where N_e is the total density of electrons and f_j, ω_j, and γ_j are the strength, frequency ($\omega_j=E_{0j}/\hbar$), and broadening of the jth transition, respectively. The f_j follows the sum rule $\Sigma_{j=1}^{q} f_j=1$. For $E\ll\hbar\omega_k$, γ_k, and taking into account that the electron density is associated with the mass density ρ through the relation $N_e=N_o(Z_t\rho/A_t)$,[53] Eq. (8) becomes

$$n^2=\varepsilon_1(E\ll E_g)=1+\left(\frac{4\pi N_o Z e^2}{mA}\sum_{j=1}^{q}\frac{f_j}{\omega_j^2}\right)\cdot\rho. \qquad (9)$$

$\Sigma_{j=1}^{q}(f_j/\omega_j^2)$ reflects the band structure of the material, through the energy values of the electronic transitions. It is very interesting that the linear relation between n^2 and ρ suggests, according to Eq. (9), that $\Sigma_{j=1}^{q}(f_j/\omega_j^2)$ remains almost the same for all CeO_x films whether they are nanocrystalline and substoichiometric (such as the EBE- and IBAD-grown films) or single crystal and stoichiometric (such as the RMS-grown film).

The most interesting and important electronic property of the materials, in order to be used in optics and optoelectronics, is the value of the fundamental gap E_g (optical-absorption edge). Therefore, the E_g values of CeO_x have attracted considerable interest.[1,10,11,20,24] The fundamental gap of CeO_x is the indirect gap of the $O2p\rightarrow Ce4f$ transition along the L high-symmetry lines of the Brillouin zone of CeO_2 (shown in Fig. 9), which is narrower than the direct gap of the same transition[20,24] and the gaps of the $O2p\rightarrow Ce5d$ and $Ce4f^0\rightarrow Ce4f^1$ transitions of CeO_2 and Ce_2O_3, respectively.[1,2,49] Using Tauc's formulation[20,38] we determined that the indirect gap of the $O2p\rightarrow Ce4f$ transition in our samples is located ~0.5-eV below the direct gap of the same transition. The fundamental gap of CeO_x films can be determined through the two-TL fittings according to Eq. (7). E_g was found to vary between 2.3 and 2.9 eV, according to the two-TL fittings. These values are much smaller than those reported in the literature.[20,24] This is a typical underestimation of E_g when the TL model is used, due to the Urbach tails in optical absorption, which are caused by defect states in the gap[36] and they are falsely taken into account by the TL fitting. However, a consistent trend of decreasing E_g with increasing Ce^{3+} content has been observed.

Another way to determine E_g is directly from the experimental ε_2 spectra following the formalism of Tauc, Grigrovici, and Vancu.[38] According to this formalism, for energies E close to E_g and for indirect electronic transitions, ε_2 follows the formula

$$E\cdot\sqrt{\varepsilon_2}\propto(E-E_g). \qquad (10)$$

This formalism is more straightforward and provides the value of E_g more accurately, without taking into account the Urbach tails. However, for thin films (such as those EBE grown at 950 °C) the multiple reflections introduce higher error in the determination of E_g. Figure 16 presents the Tauc plots of representative IBAD- and EBE-grown CeO_x films. The straight lines are linear fits with Eq. (10), through which E_g is determined. The more stoichiometric IBAD film exhibits higher E_g than the EBE film, confirming the trend of decreasing E_g with increasing Ce^{3+}, which was observed in the two-TL-fit results. The E_g values determined by the Tauc plots are higher (they vary between 2.92 and 3.12 eV) than those determined by the two-TL fits and they are in better agreement with the literature, which reports that the E_g of single crystal CeO_2 is 3.31 eV.[20]

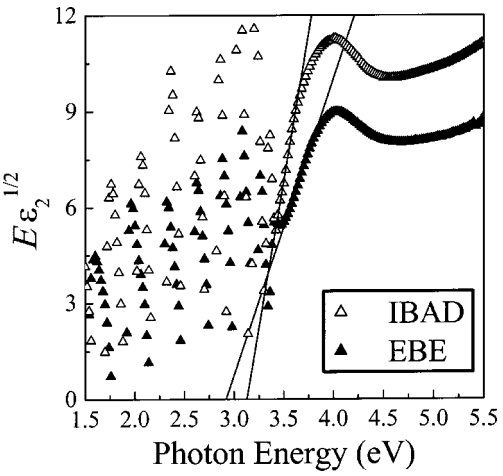

FIG. 16. Tauc plots of representative IBAD- and EBE-grown CeO_x films.

Figure 17 summarizes the variations of E_g with the $[Ce^{3+}]$ concentration, determined by both methods [two-TL fittings based on Eqs. (6) and (7) and Tauc plots based on Eq. (10)]. The RMS point is the value reported by Guo *et al.*[20] using Tauc plots. Both methods of E_g calculation show the same overall trend of decreasing E_g with increasing $[Ce^{3+}]$.

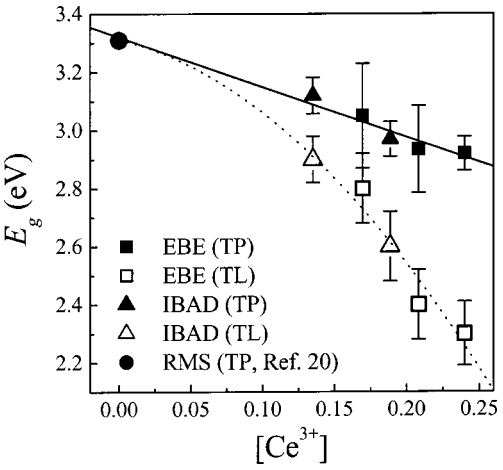

FIG. 17. The variation of the fundamental gap with the $[Ce^{3+}]$ concentration determined from SE data analysis by the two-TL fittings (TL, open symbols) and by Tauc plots (TP, solid symbols), for various growth techniques (the solid and dotted lines are guides to the eyes).

This trend is a universal behavior, since it is valid for all the used growth techniques. This is in agreement with previous works reporting that the O deficiency in CeO_2 induces an optical-absorption tail below 3 eV.[5,19] The two methods of E_g determination diverge with increasing $[Ce^{3+}]$ due to the corresponding increase of vacancy content (see Fig. 6), which enhances the gap states (due to defects) and the Urbach tails. These gap states have been proposed to be associated with O vacancies forming F centers.[5,19] In addition, in the CeO_x films of this study there exists a considerable amount of defect states due to interfaces, determined by capacitance-voltage (C-V) electrical measurements (not shown here), which may also contribute to the degradation of E_g. The strong correlation of E_g with $[Ce^{3+}]$ explains the observed redshift of E_g in nanocrystalline CeO_x.[4] The quantum-size effect is expected to enhance the band gap of the materials[29,30] due to the higher localization of energy bands with decreasing particle size (ultimately the bands are reduced to atomic states). Therefore, the redshift of E_g in nanocrystalline CeO_x films is not due to the quantum-size effect itself, but to the existence of Ce^{3+} at the grain boundaries, as we have shown in this study. Thus, the Ce^{3+} content increases, with decreasing grain size, eliminating the results of the quantum-size effect and causing the redshift of E_g.

IV. CONCLUSIONS

We have studied a variety of nanocrystalline CeO_x films grown by EBE and IBAD. Their structure, morphology, and composition have been studied in detail using XRD, XRR, and XPS. The nanocrystalline CeO_x films consist mainly of CeO_2 grains, while a considerable concentration (23%–12% at) of trivalent Ce^{3+} is distributed at the CeO_2 grain boundaries, forming amorphous Ce_2O_3. A small portion of Ce^{3+} ($<5\%$) is also located around O-vacancy sites. The bulk (surface) distribution of CeO_2 (Ce_2O_3) is a common feature of the EBE- and IBAD-grown films. The Ce_2O_3 content is explicitly correlated with the grain size due to the corresponding reduction of the surface/bulk ratio. The film density varies between 4.5 and 6.7 g/cm^3 due to the existence of voids.

We investigated the electronic properties of the various nanocrystalline CeO_x films, compared them with the data reported for epitaxial CeO_2, and established universal relations (valid for both nanocrystalline CeO_x and epitaxial CeO_2) between them and the film structure, composition, and morphology. The evaluation of the films' optical properties has been also based on previous band-structure calculations for CeO_2 and Ce_2O_3. The fundamental gap E_g of CeO_x is due to the indirect $O2p \rightarrow Ce4f$ transition along the L high-symmetry lines of the Brillouin zone and varied between 2.9 and 3.3 eV. It was correlated with the $[Ce^{3+}]$ concentration, explaining the redshift of E_g in nanostructured CeO_x, which is due to the Ce^{3+} at the grain boundaries and not the quantum-size effect itself. In addition, we observed the enhancement of the Urbach tails in optical absorption (which are associated with the vacancy content in CeO_x and therefore they are due to defect states in the gap) with increasing $[Ce^{3+}]$ and vacancy content. We also correlated the energy position of the maximum optical absorption E_{01}, due to the $O2p \rightarrow Ce4f$ electronic transition, which varies up to 160-meV wide, with the lattice constant of the CeO_2 grains. The refractive index, far below E_g, has been explicitly correlated (through the classical theory of light dispersion) with the film density, independently of the $[Ce^{3+}]$, $[Ce^{4+}]$, and $[O]$ concentrations, grain size, and the lattice parameter, showing that the density of the films is the major factor affecting n. The density was also found to be the major factor affecting the absolute, maximum value of the ε_2 peak, which corresponds to the $O2p \rightarrow Ce4f$ electronic transition. Finally, we investigated the energy location of the second Tauc-Lorentz oscillator, which averages the higher-order transitions of CeO_2 and Ce_2O_3, through fitting of its low-energy tail, and we found that its energy position is very sensitive to the film's composition, as opposed to the energy position of the $O2p \rightarrow Ce4f$ transition, which originates exclusively from CeO_2 and it is not correlated with the film composition at all.

*Electronic address: ppats@physics.auth.gr

[1] N. V. Skorodumova, R. Ahuja, S. I. Simak, I. A. Abrikosov, B. Johansson, and B. I. Lundqvist, Phys. Rev. B **64**, 115108 (2001).
[2] E. Wuilloud, B. Delley, W-D. Schneider, and Y. Baer, Phys. Rev. Lett. **53**, 202 (1984).
[3] T. Nakano, A. Kotani, and J. C. Parlebas, J. Phys. Soc. Jpn. **56**, 2201 (1987).
[4] S. Tsunekawa, T. Fukuda, and A. Kassuya, J. Appl. Phys. **87**, 1318 (2000).
[5] F. Marabelli and P. Wachter, Phys. Rev. B **36**, 1238 (1987).
[6] Y.-M. Chiang, E. B. Lavik, I. Kosacki, H. L. Tuller, and J. Y. Ying, Appl. Phys. Lett. **69**, 185 (1996).
[7] G. Atanassov, R. Thielsch, and D. Popov, Thin Solid Films **223**, 288 (1993).
[8] N. Ozer, Sol. Energy Mater. Sol. Cells **68**, 391 (2001).
[9] M. G. Krishna, A. Hartridge, and A. K. Bhattacharya, Mater. Sci. Eng., B **55**, 14 (1998).
[10] P. Patsalas, S. Logothetidis, and C. Metaxa, Appl. Phys. Lett. **81**, 466 (2002).
[11] L. Tye, N. A. El-Masry, T. Chikyow, P. McLarty, and S. M. Bedair, Appl. Phys. Lett. **65**, 3081 (1994).
[12] T. Ami and M. Suzuki, Mater. Sci. Eng., B **54**, 84 (1998).
[13] S. Gnanarajan and N. Savvides, Thin Solid Films **350**, 124 (1999).
[14] B. Hirschauer, G. Chiaia, M. Göthelid, and U. O. Karlsson, Thin Solid Films **348**, 3 (1999).
[15] T. Chikyow, S. M. Bedair, L. Tye, and N. A. El-Masry, Appl. Phys. Lett. **65**, 1030 (1994).
[16] D. P. Norton, J. D. Budai, and M. F. Chilsom, Appl. Phys. Lett. **76**, 1677 (2000).
[17] D. Huang, F. Qin, Z. Yao, Z. Ren, L. Lin, W. Gao, and Q. Ren, Appl. Phys. Lett. **67**, 3724 (1995).
[18] L. Mechin, A. Chabli, F. Bertin, M. Burdin, G. Rolland, C. Vanuffel, and J.-C. Villegier, J. Appl. Phys. **84**, 4935 (1998).

[19] A. H. Morshed, M. E. Moussa, M. Bedair, R. Leonard, S. X. Liu, and N. El-Masry, Appl. Phys. Lett. **70**, 1647 (1997).
[20] S. Guo, H. Arwin, S. N. Jacobson, K. Jarrendahl, and U. Helmersson, J. Appl. Phys. **77**, 5369 (1995).
[21] R. P. Netterfield, W. G. Sainty, P. J. Martin, and S. H. Sie, Appl. Opt. **24**, 2267 (1985).
[22] T. Inoue, Y. Yamamoto, S. Koyama, S. Suzuki, and Y. Ueda, Appl. Phys. Lett. **56**, 1332 (1990).
[23] T. Inoue, M. Osonoe, H. Tohda, M. Hiramatsu, Y. Yamamoto, A. Yamanaka, and T. Nakayama, J. Appl. Phys. **69**, 8313 (1991).
[24] K. B. Sundaram, P. F. Wahid, and P. J. Sisk, Thin Solid Films **221**, 13 (1992).
[25] L. Fangxin, W. Chengyun, S. Qingde, Z. Tianpeng, and Z. Guiwen, Appl. Opt. **36**, 2796 (1997).
[26] S. Y. Zheng, A. M. Andersson-Fäldt, B. Stjerna, and C. G. Granqvist, Appl. Opt. **32**, 6303 (1993).
[27] S. Mansour, S. Al-Robaee, K. Narasimha Rao, and S. Mohan, J. Appl. Phys. **71**, 2380 (1992).
[28] M. Veszelei, L. Kullman, C. G. Granqvist, N. Rottkay, and M. Rubin, Appl. Opt. **37**, 5993 (1998).
[29] T. W. Kim, D. C. Choo, D. U. Lee, H. S. Lee, M. S. Jang, and H. L. Park, Appl. Phys. Lett. **81**, 487 (2002).
[30] L. Bolotov, T. Tsutiya, A. Nakamura, T. Ito, Y. Fujiwara, and Y. Takeda, Phys. Rev. B **59**, 12 236 (1999).
[31] P. Patsalas and S. Logothetidis, J. Appl. Phys. **90**, 4725 (2001).
[32] P. Patsalas and S. Logothetidis, J. Appl. Phys. **88**, 6346 (2000).
[33] M. F. Toney and S. Brennan, J. Appl. Phys. **66**, 1861 (1989).
[34] D. E. Aspnes, Thin Solid Films **89**, 249 (1982).
[35] R. M. Azzam and N. M. Bashara, *Ellipsometry and Polarized Light* (North Holland, Amsterdam, 1977).
[36] G. E. Jellison and F. A. Modine, Appl. Phys. Lett. **69**, 371 (1996).
[37] D. A. G. Bruggeman, Ann. Phys. (N.Y.) **24**, 636 (1935).
[38] J. Tauc, R. Grigrovici, and A. Vancu, Phys. Status Solidi **15**, 627 (1966).
[39] F. Wooten, *Optical Properties of Solids* (Academic, New York, 1972).
[40] H. Schuster and H. Goebel, Adv. X-Ray Anal. **39**, 1 (1996).
[41] JCPDS Powder Diffraction File 43-1002 (unpublished).
[42] L. Azaroff, *The Powder Method* (Wiley, New York, 1962).
[43] P. Patsalas, C. Charitidis, and S. Logothetidis, Surf. Coat. Technol. **125**, 335 (2000).
[44] H. V. Nguyen and R. W. Collins, Thin Solid Films **233**, 272 (1993).
[45] A. Pfau and K. D. Schierbaum, Surf. Sci. **321**, 71 (1994).
[46] E. Paparazzo, G. M. Ingo, and N. Zecchetti, J. Vac. Sci. Technol. A **9**, 1416 (1991).
[47] M. Romeo, K. Bak, J. El. Fallah, F. Le Normand, and L. Hilaire, Surf. Interface Anal. **20**, 508 (1993).
[48] C. Hardacre, G. M. Roe, and R. M. Lambert, Surf. Sci. **326**, 1 (1995).
[49] D. R. Mullins, S. H. Overbury, and D. R. Huntley, Surf. Sci. **409**, 307 (1998).
[50] J. Z. Shyu, K. Otto, W. L. Watkins, G. W. Graham, R. K. Belitz, and H. S. Ganghi, J. Catal. **114**, 23 (1988).
[51] M. Niwano, S. Sato, T. Koide, T. Shidara, A. Fujimori, H. Fukutani, S. Shin, and M. Ishigame, J. Phys. Soc. Jpn. **57**, 1489 (1988).
[52] D. D. Koelling, A. M. Boering, and J. H. Wood, Solid State Commun. **47**, 227 (1983).
[53] N. W. Ashcroft and N. D. Mermin, *Solid State Physics* (Saunders, Philadelphia, 1976).